

This is the accepted manuscript made available via CHORUS. The article has been published as:

Frustration and Atomic Ordering in a Monolayer Semiconductor Alloy

Amin Azizi, Mehmet Dogan, Jeffrey D. Cain, Rahmatollah Eskandari, Xuanze Yu, Emily C. Glazer, Marvin L. Cohen, and Alex Zettl

Phys. Rev. Lett. **124**, 096101 — Published 5 March 2020

DOI: [10.1103/PhysRevLett.124.096101](https://doi.org/10.1103/PhysRevLett.124.096101)

Frustration and Atomic Ordering in a Monolayer Semiconductor Alloy

Amin Azizi^{1,2}, Mehmet Dogan^{1,3}, Jeffrey D. Cain^{1,2,3}, Rahmatollah Eskandari¹, Xuanze Yu⁴, Emily C. Glazer¹, Marvin L Cohen^{1,3}, Alex Zettl^{*,1,2,3}

1. *Department of Physics, University of California at Berkeley, Berkeley, CA, 94720, USA*
2. *Kavli Energy NanoScience Institute at the University of California, Berkeley, Berkeley, CA, 94720, USA*
3. *Materials Sciences Division, Lawrence Berkeley National Laboratory, Berkeley, CA, 94720, USA*
4. *Department of Materials Science and Engineering, University of California at Berkeley, Berkeley, CA, 94720, USA*

* Corresponding Author. E-mail: azettl@berkeley.edu , Phone: +1 (510) 642-4939 Fax: +1 (510) 642-2685

Frustrated interactions can lead to short-range ordering arising from incompatible interactions of fundamental physical quantities with the underlying lattice. The simplest example is the triangular lattice of spins with antiferromagnetic interactions, where the nearest-neighbor spin-spin interactions cannot simultaneously be energy minimized. Here we show that engineering frustrated interactions is a possible route for controlling structural and electronic phenomena in semiconductor alloys. Using aberration-corrected scanning transmission electron microscopy in conjunction with density functional theory calculations, we demonstrate atomic ordering in a two-dimensional semiconductor alloy as a result of the competition between geometrical constraints and nearest-neighbor interactions. Statistical analyses uncover the presence of short-range ordering in the lattice. In addition, we show how the induced ordering can be used as another degree of freedom to considerably modify the bandgap of monolayer semiconductor alloys.

Geometrical frustration occurs when the geometry of a system prevents its component interactions from being simultaneously satisfied, and can hinder long-range ordered ground-states [1]. Ideal frustrated systems, such as the 2D Ising model of anti-ferromagnetic spins in a triangular lattice, are characterized by degenerate ground-states and extensive entropy at zero temperature [1]. However, in real materials, the interplay between geometrical frustration and subtle effects such as lattice distortions [2,3], long-range interactions [4], and elasticity [5], can lead to relieving of frustration and formation of ordered configurations. The induced atomic ordering by frustrated interactions can be exploited as another degree of freedom to modify the material properties. In particular, ordering in multispecies alloys can significantly affect their electronic [6], optical [7], thermal [8], catalytic [9], and mechanical [10] properties.

While ordering in multispecies alloys has long been experimentally studied, most examinations have been limited to indirect methods, *e.g.* scattering techniques [11,12]. Two-dimensional (2D) materials provide an ideal platform to study atomic ordering in alloys *via* direct visualization of the lattice in real space, for example *via* scanning transmission electron microscopy (STEM). Isovalent substitutional alloying of transition metal dichalcogenides (TMDs) has been demonstrated [13,14], but they form random solid solutions due to the small formation energy (E_f) of the alloys with respect to parent materials [15]. Here, we investigate a TMD alloy consisting of transition metal elements from groups 5 and 7 and demonstrate experimental observation of atomic ordering using aberration-corrected STEM. We also suggest a general approach for controlling ordering and consequently some fundamental properties of 2D alloys through engineering frustrated nearest-neighbor interactions. Statistical analyses uncover the presence of short-range ordering in the monolayer alloy due to the interplay between geometrical frustration and Coulomb interactions. This observation is analogous to

antiferromagnetic Ising spins in a triangular lattice. Additionally, using optical spectroscopy combined with theoretical calculations, we demonstrate how the induced atomic ordering can significantly modify the alloy's bandgap.

TMD alloys consisting of non-isovalent transition metals (*e.g.* groups 5 and 7) offer rich systems for engineering their physical properties by chemical composition and layer number. In particular, monolayer ReS₂ exhibits the 1T' structure (Fig. 1a) and is a semiconductor with a bandgap of 1.43 eV [16], while monolayer NbS₂ adopts the 1H structure (Fig. 1b) and is a metal [17]. Hence, alloying ReS₂ and NbS₂ enables both phase and band structure engineering. Previous preliminary theoretical studies show that Re_xNb_{1-x}S₂ alloys can be stable [15]. In particular, Re_{0.5}Nb_{0.5}S₂ was shown to be valence isoelectronic to MoS₂ but with a smaller bandgap [15]. The fully ordered structure of Re_{0.5}Nb_{0.5}S₂, where the “different nearest-neighbor number” (DNN) (*i.e.* the number of nearest neighbors of the other kind) is 4, is shown in Fig. 1c. If the atomic species Re and Nb were randomly distributed, the average DNN ($\overline{\text{DNN}}$) would be 3.

In this work we theoretically and experimentally examine Re_xNb_{1-x}S₂ alloys and demonstrate that the synthesized Re_{0.5}Nb_{0.5}S₂ alloy possesses a $\overline{\text{DNN}}$ between the random and the fully ordered alloys due to the competition between the drives toward satisfying a higher portion of the nearest-neighbor interactions and higher entropy. We first expand upon previous theoretical predictions using larger simulation cells. Total energy calculations of Re_xNb_{1-x}S₂ as a function of composition reveal a phase transition from 1H to 1T' at $x = 0.68$ (Fig. 1d). Knowing the ground state phase for each composition, we compute the formation energies (E_f) with respect to the two parent TMD components (Fig. 1e) (see Supplemental Material). We find that the alloys are stable up to $x = 0.63$ with the $x = 0.50$ alloy being the most stable. The high

stability of $\text{Re}_{0.5}\text{Nb}_{0.5}\text{S}_2$ can be attributed to the equal mixing of Re and Nb, which have one more and one fewer valence electron than Mo, respectively. Alloying also enables bandgap engineering of $\text{Re}_x\text{Nb}_{1-x}\text{S}_2$. Figure 1f presents the composition-dependent bandgap of monolayer $\text{Re}_x\text{Nb}_{1-x}\text{S}_2$ in the 1H and 1T' phases. It shows a broad range of bandgaps, from metallic ($x = 0$, NbS_2) to semiconducting ($x = 1$, ReS_2), in contrast to a limited bandgap range offered by isovalent TMD alloys [8,14,18]. Particularly, the monolayer $\text{Re}_{0.5}\text{Nb}_{0.5}\text{S}_2$ displays a bandgap of 1.15 eV (1.08 eV with spin-orbit interaction (SOI) included). Additionally, the Coulomb interaction between Re and Nb atoms with different charge states leads to correlated nearest-neighbor pairs. Equal numbers of Re and Nb atoms in such a system can be easily distributed in a square lattice while satisfying the nearest-neighbor interactions (*i.e.* an unfrustrated system (Fig. 1g)). However, it is not possible to simultaneously satisfy all interactions in a triangular lattice like the transition metal sub-lattice in $\text{Re}_{0.5}\text{Nb}_{0.5}\text{S}_2$, and hence such a system is frustrated (Fig. 1h). The presence of frustrated interactions in $\text{Re}_{0.5}\text{Nb}_{0.5}\text{S}_2$, in addition to it having the lowest formation energy among all $\text{Re}_x\text{Nb}_{1-x}\text{S}_2$ and being valence isoelectronic to MoS_2 , make it an intriguing system to explore experimentally.

We synthesize bulk single crystals of $\text{Re}_{0.5}\text{Nb}_{0.5}\text{S}_2$ with a layered structure that can be easily exfoliated (Fig. S1). The alloy is air-stable and the samples are exfoliated under ambient conditions. Figure 2a shows an aberration-corrected annular dark-field scanning transmission electron microscope (ADF-STEM) image of the monolayer $\text{Re}_{0.5}\text{Nb}_{0.5}\text{S}_2$. The fast Fourier transform (FFT) (inset) reveals the hexagonal symmetry of the lattice as expected from the total energy calculations. Owing to the Z-contrast mechanism in ADF-STEM images, brighter and dimmer spots correspond to Re and Nb atoms, respectively. Chemical composition directly

extracted from the ADF-STEM image confirms near-equal concentration of Re and Nb within the lattice (*i.e.* $\text{Re}_{0.51}\text{Nb}_{0.49}\text{S}_2$).

The most striking structural feature of $\text{Re}_{0.5}\text{Nb}_{0.5}\text{S}_2$ is the formation of meandering transition metal stripes. This is quite distinct from the atomic structure of other 2D TMD alloys reported to date. It suggests $\text{Re}_{0.5}\text{Nb}_{0.5}\text{S}_2$ has short-range order, in sharp contrast to the random structure of the isovalent TMD alloys [13,14,19]. This can be attributed to the small formation energy of the group 6 TMD alloys (~ 2 meV/atom [15]) compared to the formation energy of about -70 meV/atom for $\text{Re}_{0.5}\text{Nb}_{0.5}\text{S}_2$. To verify the presence of atomic ordering, we perform statistical analysis on multiple ADF-STEM images. A representative image and its filtered counterpart highlighting the meandering atomic stripes formed by Re atoms are shown in Figs. 2b-c. Figure 2d presents the probabilities of having DNN values of 1 through 6. It shows that the majority of metal atoms have 4 nearest neighbors of the other kind with a $\overline{\text{DNN}}$ of 3.82, very different from the $\overline{\text{DNN}}$ of 3 for a random distribution. This preference to be adjacent to the other atomic species is analogous to antiferromagnetic Ising spins, which leads to geometrical frustration in a triangular lattice [1]. In such a system, there is an energy cost for having two parallel spins as nearest neighbors, yet it is not possible to have all nearest-neighbor pairs be anti-parallel. This lattice can be thought of as consisting of triangles in which each nearest-neighbor interaction is part of only one triangle (Fig. S5). If all the triangles have at least (and only) one pair of parallel spins, the energy is minimized. In our system, up and down spins correspond to Nb and Re atoms, and the triangular lattice is the transition metal sub-lattice. The parameter that we call $\overline{\text{DNN}}$ is related to the Warren–Cowley short-range order (SRO) parameter [8,20] α via the simple relation $\alpha = 1 - \frac{\overline{\text{DNN}}}{3}$, for the case of a triangular lattice in which the lattice sites are occupied with two different kinds of atoms with equal probability. We

note that the sizes of the Nb and Re atoms in the lattice are similar (computed NbS₂ and ReS₂ lattice constants in the 1H phase are 3.34 Å and 3.19 Å, respectively), and they constitute an almost perfect triangular lattice with distortions smaller than a few picometers regardless of the atomic species distribution (see Supplemental Material). Therefore, the heteroatomic tendency cannot be attributed to this size difference. Additionally, the experimental and computed lattice constants for the monolayer Re_{0.5}Nb_{0.5}S₂ are 3.35 Å and 3.22 Å, respectively (a match to within 4%).

We also calculate the spatial correlation functions along three zigzag directions (see Supplemental Material). A positive (negative) value for the correlation function corresponds to the fact that the pair of sites tend to be homoatomic (heteroatomic), whereas a value of zero indicates that the sites are uncorrelated. Figure 2e shows that the correlation for the nearest neighbors in all zigzag directions is between 0 and -0.1 with an average of -0.068 ± 0.022 . The value being negative indicates a tendency for the alloy to form heteroatomic nearest-neighbor coordination. The correlation goes to zero beyond the first nearest neighbors, suggesting the lack of long-range order.

The statistical analyses are extended by examining the lengths of homoatomic stripes along the zigzag directions. Figure 2f contains histograms of the stripe length along the three zigzag directions extracted from the ADF-STEM image in Fig. 2b. The nearly similar length distribution of the homoatomic stripes along all three directions suggests that the monolayer alloy is also isotropic.

The DNN and correlation data presented in Figs. 2d-e suggest that a nearest-neighbor-based model may be applicable to explain the preferred distribution of atomic species. To build such a model, we run 60 simulations including 12 experimental and 12 random 6×6

configurations. For each simulation, we compute the $\overline{\text{DNN}}$ and relax all the atomic coordinates to find the total energy. Figure 3a presents the results where the energy of the reference structure shown in Fig. 1c is taken as zero. The fact that a linear fit is possible suggests that a nearest-neighbor model where the energy cost of having neighbors of the same (different) kind is 0 eV (-0.15) eV should be a faithful representation of this system.

To explore the thermodynamics of species distribution at finite temperature in the alloys, we solve a nearest-neighbor model using Monte Carlo simulations [21,22]. The simulated $\overline{\text{DNN}}$ for temperatures ranging from 11.6 K to 3.8×10^5 K is shown in Fig. 3b. We choose this wide temperature range to explore the full range of behavior within our model, even though the actual material would not stay solid at such high temperatures. At each temperature, ten simulations are run, and the plotted values reflect the averages and the standard deviations among those runs. It is observed that, at low temperatures, the $\overline{\text{DNN}}$ is equal to its upper bound of 4 ($\alpha = -\frac{1}{3}$), and at high temperatures, it approaches 3 as the distribution becomes random ($\alpha = 0$). This transition occurs gradually at temperatures of the order of the nearest-neighbor interaction energy (0.15 eV or 1740 K). This agrees with the studies of antiferromagnetic Ising spins in a triangular lattice [1,23].

Figure 3c presents a well-thermalized instance of a simulation run at $k_{\text{B}}T = 0.105$ eV ($T = 1220$ K), which is in the range of the temperature at which the crystal is grown. The spatial correlation functions and DNN probability distribution extracted from the low-temperature nearest-neighbor model (Fig. 3c) agree well with the averaged data extracted from several experimental images (Fig. 3d). To show how the configuration with short-range atomic order compares with a random configuration, a sample 20×20 supercell where a randomly-chosen half of the sites are occupied with Nb and the other half with Re is demonstrated in Fig. 3e.

Quantifying the spatial correlation functions and DNN probability distribution for the random configuration (Fig. 3e) clearly differentiates it from the observed experimental atomic structure of $\text{Re}_{0.5}\text{Nb}_{0.5}\text{S}_2$.

The 2D materials offer a potentially lucrative playground for bandgap engineering not only by alloy composition [14] but also by layer number [24]. Here, we show that, in addition to the composition and layer number, induced atomic ordering can be used to engineer the bandgap of layered semiconductor alloys. The bandgap of the reference configuration (Fig. 1c) is found to be 1.15 eV in a no-SOI calculation (Fig. 1f). However, in the real alloy such long-range order is not present. In order to investigate the effects of the atomic species distribution, we compute the bandgaps of 12 6×6 configurations taken from the ADF-STEM images as well as 12 random 6×6 configurations. Figure 4a displays the bandgap versus total energy. The results can be summarized in three main observations: (i) The experimental and random configurations are clearly separated in terms of both total energy and bandgap. (ii) The bandgap is negatively correlated with the total energy, and hence with the randomness. This has previously been observed in $\text{W}_{0.5}\text{Mo}_{0.5}\text{S}_2$ to a lesser degree [8]. (iii) For the experimental configurations, the bandgap values average to 0.70 ± 0.18 eV. Such a large spread is unusual and points to the importance of the atomic distribution at the smallest scale in determining the electronic structure of these systems.

Fourier transform infrared (FTIR) spectroscopy is used to measure the bandgap of $\text{Re}_{0.5}\text{Nb}_{0.5}\text{S}_2$ with different layer numbers. We obtain absorption spectra (Fig. 4b) from the transmission and reflection measurements. A red-shift in the onset of the absorption and an increase in the absorption peak with increasing thickness can be clearly seen. The absorption spectrum for the monolayer $\text{Re}_{0.5}\text{Nb}_{0.5}\text{S}_2$ suggests a bandgap of ~ 1.03 eV, which is in the range

of the computed bandgaps for the experimental configurations and considerably different from that of the random configurations. We further explore the dependence of bandgap on the $\text{Re}_{0.5}\text{Nb}_{0.5}\text{S}_2$ thickness. Figure 4c summarizes the experimental and computed bandgap as a function of layer number. Experimental and theoretical results are in well agreement, suggesting a reduction of bandgap from ~ 1.03 eV to ~ 0.36 eV when the thickness increases from a monolayer to bulk. This is a very useful bandgap range for which there is currently a need for air-stable 2D materials. Additionally, the bandgap of the monolayer alloy is similar to that of silicon (~ 1.1 eV) that enables fabrication of functional heterostructures and devices.

We have demonstrated a promising avenue for controlling atomic ordering in semiconductor alloys by engineering frustrated interactions as an effective approach to tune their fundamental properties. Additionally, we find a quantitative connection between frustrated interactions and ordering of atomic species in a crystal lattice, and the 2D Ising model of antiferromagnetically-coupled spins in a triangular lattice. Based on our model, further work to synthesize $\text{Re}_{0.5}\text{Nb}_{0.5}\text{S}_2$ at lower temperatures might result in a $\overline{\text{DNN}}$ closer to 4 (*i.e.* $\overline{\text{DNN}}$ is expected to increase as the growth temperature decreases). This enables to control the degree of ordering and the resulting electrical, optical, and thermal properties.

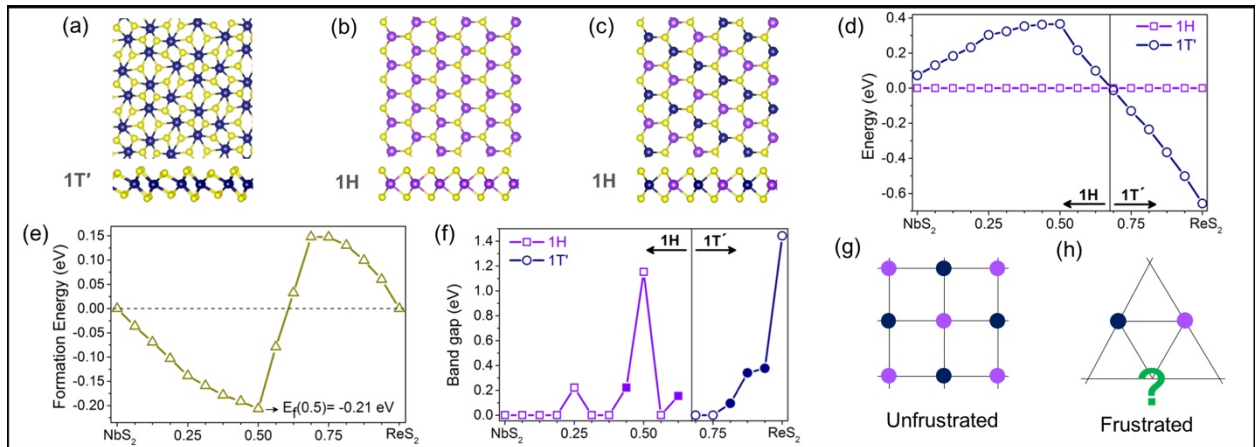


Fig. 1. Monolayer $\text{Re}_x\text{Nb}_{1-x}\text{S}_2$. Top and side view models of monolayer (a) ReS_2 , (b) NbS_2 , and (c) $\text{Re}_{0.5}\text{Nb}_{0.5}\text{S}_2$. (d) Total energies of the 1T' structure with respect to the 1H structure. (e) Compositional formation energy of the lowest-energy phase with respect to the parent TMDs. (f) Computed composition-dependent bandgaps for $\text{Re}_x\text{Nb}_{1-x}\text{S}_2$. Filled points indicate a direct gap and energies are reported in eV/ MS_2 . (g) An unfrustrated system with a square lattice versus (h) a frustrated system with a triangular lattice.

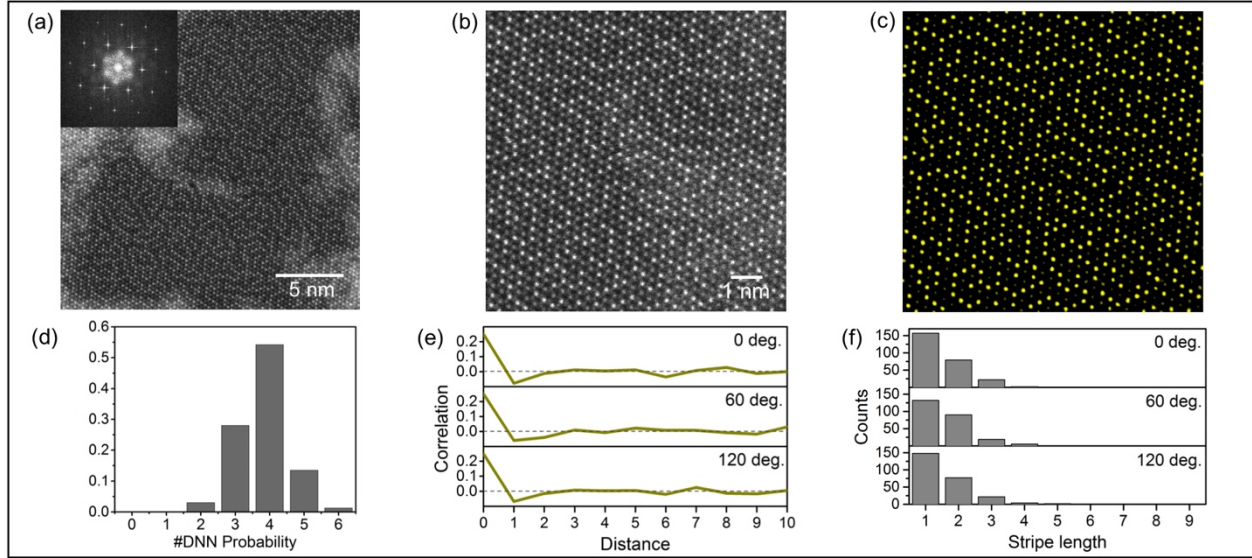


Fig. 2. Atomic ordering in monolayer $\text{Re}_{0.5}\text{Nb}_{0.5}\text{S}_2$. (a) An ADF-STEM image of the monolayer $\text{Re}_{0.5}\text{Nb}_{0.5}\text{S}_2$ with the corresponding FFT (inset). (b) A higher magnification ADF-STEM image of $\text{Re}_{0.5}\text{Nb}_{0.5}\text{S}_2$ used for statistical analyses and (c) its filtered version. (d) Probability distribution of DNN, (e) spatial correlation functions in the three zigzag directions, and (f) histograms of homoatomic stripe lengths for a 20×20 unit cell portion of the image presented in (b).

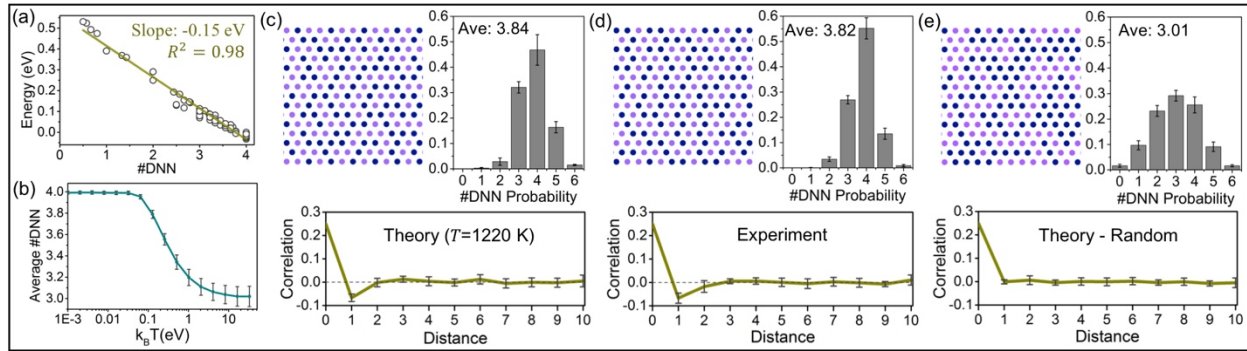


Fig. 3. Nearest-neighbor-based model describing the preferred distribution of atomic species. (a) DFT total energies of 60 $\text{Re}_{0.5}\text{Nb}_{0.5}\text{S}_2$ configurations and Nb-Re distributions versus their $\overline{\text{DNN}}$. Energies are reported in eV/ MS_2 and the best fit line is shown. R^2 stands for the coefficient of determination, and is close to 1, indicating that the linear fit closely represents the data. (b) $\overline{\text{DNN}}$ versus temperature in the nearest-neighbor model solved by Monte Carlo simulations. A portion of the Nb-Re distribution (c) obtained by the Monte Carlo simulations at $T = 1220$ K, (d) extracted from the image in Fig. 2b, and (e) for a random configuration, as well

as the average probability distribution of DNN and the averaged correlation function for four such configurations. (Re: navy, Nb: light violet)

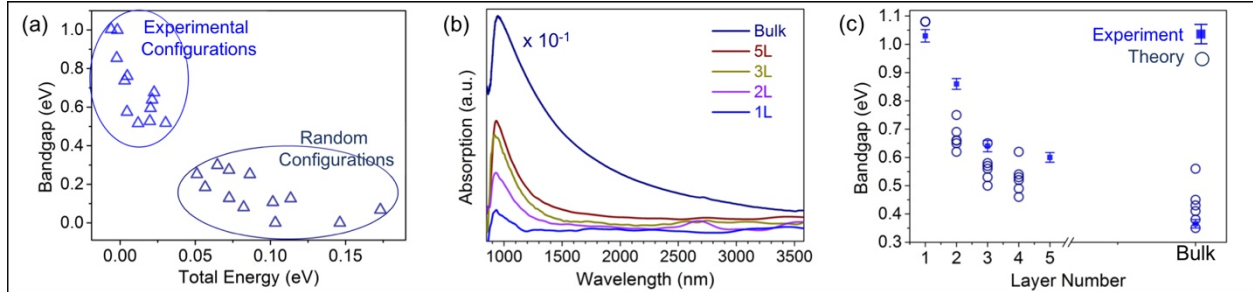


Fig. 4. Bandgap tunability of $\text{Re}_{0.5}\text{Nb}_{0.5}\text{S}_2$ by ordering and layer number. (a) DFT bandgaps versus DFT total energies for 12 experimental and 12 random configurations. Energies are reported in eV/ MS_2 and the energy of the reference structure (Fig. 1c) is taken as zero. (b) Optical absorption spectra of $\text{Re}_{0.5}\text{Nb}_{0.5}\text{S}_2$ as a function of layer number. The intensity of the spectrum for bulk $\text{Re}_{0.5}\text{Nb}_{0.5}\text{S}_2$ is divided by 10. (c) Experimental and theoretical band gaps versus the $\text{Re}_{0.5}\text{Nb}_{0.5}\text{S}_2$ thickness. For the experimental values, several measurements are performed on each flake and the error bars represent standard deviation. For the theoretical values, the monolayer alloy shown in Fig. 1c is taken as the reference structure, and multiple high-symmetry stacking sequences with lowest energy are used for calculations of bandgap for the multilayer alloys. SOI is included.

Acknowledgements The experimental portion of this work was supported primarily by the Director, Office of Science, Office of Basic Energy Sciences, Materials Sciences and Engineering Division, of the U.S. Department of Energy under contract No. DE-AC02-05-CH11231, within the van der Waals Heterostructures Program (KCWF16), which provided for synthesis of the material, STEM characterization, and image statistical analysis. Support was also provided by the National Science Foundation Grant No. DMR-1807233 which provided for additional sample characterization. The theoretical (MD and MLC) portion of this work was supported primarily by the Director, Office of Science, Office of Basic Energy Sciences, Materials Sciences and Engineering Division, of the U.S. Department of Energy under contract No. DE-AC02-05-CH11231, within the sp^2 -bonded Materials Program (KC2207), which provided for total energy and bandgap calculations. Support for the theoretical work (MD and MLC) which involved the analytic modelling of the alloy systems was provided by the NSF Grant No. DMR-1926004. Computational resources were provided by the DOE at Lawrence Berkeley National Laboratory’s NERSC facility and the NSF through XSEDE resources at NICS. We also gratefully acknowledge the facilities and technical support provided by Hans A.

Bechtel and the Advanced Light Source at Lawrence Berkeley National Laboratory, and thank Sehoon Oh for fruitful scientific discussions.

REFERENCES

- [1] G. H. Wannier, Phys. Rev. **79**, 357 (1950).
- [2] L. Gu, B. Chakraborty, P. L. Garrido, M. Phani, and J. L. Lebowitz, Phys. Rev. B **53**, 11985 (1996).
- [3] Y. Han, Y. Shokef, A. M. Alsayed, P. Yunker, T. C. Lubensky, and A. G. Yodh, Nature **456**, 898 (2008).
- [4] B. D. Metcalf, Phys. Lett. A **46**, 325 (1974).
- [5] S. H. Kang, S. Shan, A. Košmrlj, W. L. Noorduin, S. Shian, J. C. Weaver, D. R. Clarke, and K. Bertoldi, Phys. Rev. Lett. **112**, 098701 (2014).
- [6] K. A. Mäder and A. Zunger, Phys. Rev. B **51**, 10462 (1995).
- [7] J. E. Bernard, S. -H. Wei, D. M. Wood, and A. Zunger, Appl. Phys. Lett. **52**, 311 (1988).
- [8] A. Azizi, Y. Wang, Z. Lin, K. Wang, A. L. Elias, M. Terrones, V. H. Crespi, and N. Alem, Nano Lett. **16**, 6982 (2016).
- [9] D. Wang, H. L. Xin, R. Hovden, H. Wang, Y. Yu, D. A. Muller, F. J. DiSalvo, and H. D. Abruña, Nat. Mater. **12**, 81 (2013).
- [10] Z. Lei, X. Liu, Y. Wu, H. Wang, S. Jiang, S. Wang, X. Hui, Y. Wu, B. Gault, P. Kontis, D. Raabe, L. Gu, Q. Zhang, H. Chen, H. Wang, J. Liu, K. An, Q. Zeng, T.-G. Nieh, and Z. Lu, Nature **563**, 546 (2018).
- [11] M. A. Shahid, S. Mahajan, D. E. Laughlin, and H. M. Cox, Phys. Rev. Lett. **58**, 2567 (1987).
- [12] G. B. Stringfellow, J. Vac. Sci. Technol. B Microelectron. Nanom. Struct. **9**, 2182 (1991).
- [13] D. O. Dumcenco, H. Kobayashi, Z. Liu, Y.-S. Huang, and K. Suenaga, Nat. Commun. **4**, 1351 (2013).
- [14] Y. Chen, J. Xi, D. O. Dumcenco, Z. Liu, K. Suenaga, D. Wang, Z. Shuai, Y.-S. Huang, and L. Xie, ACS Nano **7**, 4610 (2013).
- [15] T. L. Tan, M.-F. Ng, and G. Eda, J. Phys. Chem. C **120**, 2501 (2016).
- [16] S. Tongay, H. Sahin, C. Ko, A. Luce, W. Fan, K. Liu, J. Zhou, Y.-S. Huang, C.-H. Ho, J. Yan, D. F. Ogletree, S. Aloni, J. Ji, S. Li, J. Li, F. M. Peeters, and J. Wu, Nat. Commun. **5**,

- 3252 (2014).
- [17] X. Wang, J. Lin, Y. Zhu, C. Luo, K. Suenaga, C. Cai, and L. Xie, *Nanoscale* **9**, 16607 (2017).
 - [18] J. Mann, Q. Ma, P. M. Odenthal, M. Isarraraz, D. Le, E. Preciado, D. Barroso, K. Yamaguchi, G. von Son Palacio, A. Nguyen, T. Tran, M. Wurch, A. Nguyen, V. Klee, S. Bobek, D. Sun, T. F. Heinz, T. S. Rahman, R. Kawakami, and L. Bartels, *Adv. Mater.* **26**, 1399 (2014).
 - [19] L.-Y. Gan, Q. Zhang, Y.-J. Zhao, Y. Cheng, and U. Schwingenschlögl, *Sci. Rep.* **4**, 6691 (2014).
 - [20] A. K. Engstfeld, H. E. Hoster, R. J. Behm, L. D. Roelofs, X. Liu, C.-Z. Wang, Y. Han, and J. W. Evans, *Phys. Rev. B* **86**, 085442 (2012).
 - [21] N. Metropolis, A. W. Rosenbluth, M. N. Rosenbluth, A. H. Teller, and E. Teller, *J. Chem. Phys.* **21**, 1087 (1953).
 - [22] M. Dogan and S. Ismail-Beigi, *J. Phys. Chem. C* **123**, 14350 (2019).
 - [23] Y. Saito and K. Igeta, *J. Phys. Soc. Japan* **53**, 3060 (1984).
 - [24] A. Azizi, G. Antonius, E. Regan, R. Eskandari, S. Kahn, F. Wang, S. G. Louie, and A. Zettl, *Nano Lett.* **19**, 1782 (2019).
 - [25] See Supplemental Material at [\[url\]](#) for Materials and Methods, Supplementary Text, Supplementary Figures, and Supplementary Table. The Supplemental Material includes Refs. [26-34].
 - [26] A. Azizi, X. Zou, P. Ercius, Z. Zhang, A. L. Elías, N. Perea-López, G. Stone, M. Terrones, B. I. Yakobson, and N. Alem, *Nat. Commun.* **5**, 4867 (2014).
 - [27] A. M. van der Zande, P. Y. Huang, D. a Chenet, T. C. Berkelbach, Y. You, G.-H. Lee, T. F. Heinz, D. R. Reichman, D. a Muller, and J. C. Hone, *Nat. Mater.* **12**, 554 (2013).
 - [28] A. Azizi, S. Eichfeld, G. Geschwind, K. Zhang, B. Jiang, D. Mukherjee, L. Hossain, A. F. Piasecki, B. Kabius, J. A. Robinson, and N. Alem, *ACS Nano* **9**, 4882 (2015).
 - [29] A. Azizi, Y. Wang, G. Stone, A. L. Elias, Z. Lin, M. Terrones, V. H. Crespi, and N. Alem, *Nano Lett.* **17**, 2802 (2017).
 - [30] J. P. Perdew, K. Burke, and M. Ernzerhof, *Phys. Rev. Lett.* **77**, 3865 (1996).
 - [31] P. Giannozzi, S. Baroni, N. Bonini, M. Calandra, R. Car, C. Cavazzoni, D. Ceresoli, G. L. Chiarotti, M. Cococcioni, I. Dabo, A. Dal Corso, S. de Gironcoli, S. Fabris, G. Fratesi, R.

- Gebauer, U. Gerstmann, C. Gougoussis, A. Kokalj, M. Lazzeri, L. Martin-Samos, N. Marzari, F. Mauri, R. Mazzarello, S. Paolini, A. Pasquarello, L. Paulatto, C. Sbraccia, S. Scandolo, G. Sclauzero, A. P. Seitsonen, A. Smogunov, P. Umari, and R. M. Wentzcovitch, *J. Phys. Condens. Matter* **21**, 395502 (2009).
- [32] N. Marzari, D. Vanderbilt, A. De Vita, and M. C. Payne, *Phys. Rev. Lett.* **82**, 3296 (1999).
- [33] S. Grimme, *J. Comput. Chem.* **27**, 1787 (2006).
- [34] V. Barone, M. Casarin, D. Forrer, M. Pavone, M. Sambi, and A. Vittadini, *J. Comput. Chem.* **30**, 934 (2009).